Retraction

Retracted: Extraction and Visualization of Ocular Blood Vessels in 3D Medical Images Based on Geometric Transformation Algorithm

Journal of Healthcare Engineering

This article has been retracted by Hindawi following an investigation undertaken by the publisher [1]. This investigation has uncovered evidence of one or more of the following indicators of systematic manipulation of the publication process:

(1) Discrepancies in scope

(2) Discrepancies in the description of the research reported

(3) Discrepancies between the availability of data and the research described

(4) Inappropriate citations

(5) Incoherent, meaningless and/or irrelevant content included in the article

(6) Peer-review manipulation

The presence of these indicators undermines our confidence in the integrity of the article's content and we cannot, therefore, vouch for its reliability. Please note that this notice is intended solely to alert readers that the content of this article is unreliable. We have not investigated whether authors were aware of or involved in the systematic manipulation of the publication process. Wiley and Hindawi regrets that the usual quality checks did not identify these issues before publication and have since put additional measures in place to safeguard research integrity.

We wish to credit our own Research Integrity and Research Publishing teams and anonymous and named external researchers and research integrity experts for contributing to this investigation.

The corresponding author, as the representative of all authors, has been given the opportunity to register their agreement or disagreement to this retraction. We have kept a record of any response received.

References

[1] Z. Zhang, S. Zhang, and H. Feng, "Extraction and Visualization of Ocular Blood Vessels in 3D Medical Images Based on Geometric Transformation Algorithm," *Journal of Healthcare Engineering*, vol. 2021, Article ID 5573381, 13 pages, 2021.

Research Article

Extraction and Visualization of Ocular Blood Vessels in 3D Medical Images Based on Geometric Transformation Algorithm

Zhike Zhang,[1] Shuixin Zhang,[2] and Hongyu Feng [3]

[1]*Department of Ophthalmology, China-Japan Friendship Hospital, Beijing 100029, China*
[2]*Department of Traditional Chinese Medicine, Haidian Traditional Chinese Medical Hospital, Beijing 100080, China*
[3]*Henan Institute of Science and Technology, Xinxiang 453003, Henan, China*

Correspondence should be addressed to Hongyu Feng; fyr@hist.edu.cn

Data extraction and visualization of 3D medical images of ocular blood vessels are performed by geometric transformation algorithm, which first performs random resonance response in a global sense to achieve detection of high-contrast coarse blood vessels and then redefines the input signal as a local image shielding the global detection result to achieve enhanced detection of low-contrast microfine vessels and complete multilevel random resonance segmentation detection. Finally, a random resonance detection method for fundus vessels based on scale decomposition is proposed, in which the images are scale decomposed, the high-frequency signals containing detailed information are randomly resonantly enhanced to achieve microfine vessel segmentation detection, and the final vessel segmentation detection results are obtained after fusing the low-frequency image signals. The optimal stochastic resonance response of the nonlinear model of neurons in the global sense is obtained to detect the high-grade intensity signal; then, the input signal is defined as a local image with high-contrast blood vessels removed, and the parameters are optimized before the detection of the low-grade intensity signal. Finally, the multilevel random resonance response is fused to obtain the segmentation results of the fundus retinal vessels. The sensitivity of the multilevel segmentation method proposed in this paper is significantly improved compared with the global random resonance results, indicating that the method proposed in this paper has obvious advantages in the segmentation of vessels with low-intensity levels. The image library was tested, and the experimental results showed that the new method has a better segmentation effect on low-contrast microscopic blood vessels. The new method not only makes full use of the noise for weak signal detection and segmentation but also provides a new idea of how to achieve multilevel segmentation and recognition of medical images.

1. Introduction

The retinal vascular network is the only vascular system that can be visualized and photographed in vivo. Retinal vascular imaging can provide clinical prognostic information for patients suffering from specific cardiovascular and ophthalmic diseases [1]. Segmentation of the retinal vasculature is a prerequisite for monitoring the status of the retinal vascular network [2]. Currently, retinal vascular segmentation is highly dependent on manual work by experienced ophthalmologists, which is tedious, time-consuming, and has low reproducibility. Therefore, a fully automated and accurate retinal vessel segmentation method is urgently needed to reduce the workload of ophthalmologists and provide objective, accurate measurements of retinal vessel abnormalities [3]. There are many small blood vessels in the fundus image, and the only ones that can be directly visualized noninvasively are the deeper blood vessels in the body [4]. Age-related macular degeneration, among other eye diseases, is also closely associated with diseases such as hypertension, atherosclerosis, and diabetes. Segmenting blood vessels and extracting blood vessel features from fundus images are very important to improve the convenience when visiting patients, so that doctors can quickly diagnose and find diseases and improve diagnosis efficiency. In addition to its medical importance, the study of fundus vascular imaging is also an important reference in biometric identification [5]. By extracting and detecting retinal blood

vessels and measuring and analysing the relevant features of blood vessels such as width, angle, and degree of curvature, several diseases mentioned above can be analysed and predicted to a great extent and used as a basis for the diagnosis of relevant diseases so that scientific disease prevention and corresponding drug treatment can be carried out [6]. Not only that, with the acquisition of enough data, it is possible to achieve more accurate and rapid assisted diagnostic decisions for ophthalmic diseases, driven by massive data [7]. On the other hand, if we do not use computer-aided technology to segment the retinal vessels in the fundus, we can only rely on the doctors' own experience to perform subjective segmentation of the vessels, but the subjective segmentation is time-consuming and inefficient, and the accuracy is low, and the subjectivity is too strong [8]. Different doctors often give different segmentation results for the same fundus image, and even the same doctor will give different results for the same fundus image before and after two different segmentation tests. The absence of an objective segmentation result can cause great problems for the patient's smooth follow-up [9].

Alam et al. proposed an adaptive detection-deletion mechanism for vessel tracking detection, in which a one-dimensional filter defines the tracking path, and the segmented detected vessel segments are removed from the film to prevent overlapping detection, and the next tracking starting point is found from the remaining vessel branches, and the cycle is iterated to complete the detection [10]. Motta et al. proposed a multiscale line tracking method with morphological assistance, in which the brightest points in the image pixels are selected as the initial seed points for tracking until the vessel profile does not satisfy the tracking conditions [11]. Lee et al. proposed a blood vessel tracking method based on Bayesian theory and multiscale linear detection by considering all the features of blood vessel intersection and branching points as well as the cross-sectional direction and vertical grayscale profile of blood vessels [12]. However, such methods can generally segment and detect only some local information on blood vessels, and their tracking paths are easily interrupted by branch points and intersections, resulting in inaccurate segmentation results [13]. Zhang et al. used the Kirsch operator as the convolution kernel for matched filtering, but its segmentation detection effect in microscopic blood vessels with low contrast is still not obvious, and there are voids in the middle of the segmented detected blood vessels [14]. Rocha et al. used Gabor transform to manipulate fundus images to extract pixels and regions that match the vessel features to obtain segmentation detection results, but the implementation process needs to be supplemented with a large number of presegmented standard images, and in most cases, there are insufficient conditions for implementation [15]. Joseph et al. used a simple pulse-coupled neural network and a fast 2D Otsu threshold segmentation method combined with a distributed genetic algorithm to extract the main blood vessels and proposed a method to automatically detect the retinal blood vessels in the fundus [16]. Such methods usually require a large computational effort and are generally poorly resistant to interference and prone to misdetection [17].

To sum up, the current auxiliary diagnostic systems often have problems such as slow computing and inaccurate calculation, and doctors do not dare to hand over patients directly to the auxiliary diagnostic systems. The system often appears as an auxiliary tool for the doctor. Only by significantly improving the diagnostic accuracy of the auxiliary diagnostic system will it be possible to achieve commercial use in the future. The use of such an intelligent diagnostic system in clinical medicine will not only significantly improve the diagnostic accuracy but also effectively solve the problem of a severe shortage of glaucoma-related experts. Therefore, in recent years, the optic cup segmentation of fundus images has received much attention in research related to the diagnosis of retinal optic nerve diseases. The methods summarized and classified above have made great contributions to the detection of fundus retinal vessel segmentation and provided multidimensional divergent ideas for research in this field, but overall there are still certain limitations in each method, such as excessive computation, poor anti-interference ability, too narrow adaptive range, and so on, which make the field still have a lot of space to explore. Most of the existing methods for fundus vessel segmentation still cannot solve the problems well, including too many prerequisites for algorithm implementation, too many limitations, unsatisfactory results for detection of vessel centreline highlighting and focal areas, poor performance for detection of low-contrast microvessels at the edge of the optic disc, poor accuracy of vessel centreline extraction, which cannot meet the purpose of clinical medicine, etc. Therefore, this paper focuses on solving the problem of poor detection performance of low-contrast microvessels by introducing stochastic resonance theory mechanism, hoping to improve the detection performance of microvessels in fundus retinal images and to provide new ideas for research in this field.

2. Geometric Transformation Algorithms for Image Extraction and Visualization Analysis

2.1. Geometric Transformation Algorithm Design. We generally must go through a preprocessing step of medical image data before performing medical image alignment, the reasons for which can be summarized as follows: the acquired images usually still have a large amount of noise due to the influence of different factors. Other original information is inserted in the image. In general, medical images have high dimensional features [18]. The main purpose of medical image preprocessing [19] is to improve the quality of medical images so that the preprocessed medical images have more features that can be easily detected compared to the original images, which facilitates feature extraction algorithms to extract more features. Compared with other images, the image information contained in medical images is more unique in the medical field. Medical images exhibit more textures and higher resolutions than ordinary images, which require more correlation and storage space, and are also more reliable for clinical applications; therefore, they have higher requirements for the relevant medical image alignment algorithms. Also, the quality of medical images

can be seriously affected during the process of medical image acquisition, transmission, and format conversion. For example, changes in image grayscale values, noise, and geometric distortion, as well as the loss of image details can reduce image information and even lead to errors.

In image alignment, the source of image data and the goodness of the data have a very important connection with the robustness and applicability of the developed image alignment algorithm, while the presence of some useless information (i.e., not of interest to the researcher) in the image can have an impact on the accuracy of the image alignment algorithm. However, during the implementation of most image alignment algorithms, we found that they did not preprocess the images, which would lead them to affect the accuracy of the algorithms in subsequent steps such as feature extraction and matching. Image preprocessing usually aims to reduce some image useless information (e.g., noise) in the image as much as possible and recover more realistic information in the image as a way to simplify the data information in the image so that more useful information can be efficiently used by the researcher. In short, it enhances the image data quality by suppressing unnecessary distortions and enhancing the desired image features. The preprocessing process of medical images directly affects the accuracy of subsequent medical image alignment algorithms. Therefore, it is necessary to preprocess the images before image alignment so that not only the image quality can be improved, but also the realism of medical images will not be affected, as shown in Figure 1.

We generally accomplish retinal image alignment indirectly by aligning two feature point sets. In this process, it is necessary to extract appropriate and effective image feature information to represent the image since our goal aims to ensure the robustness and accuracy of image alignment [19]. Therefore, in this paper, preference is given to invariant, unique, and highly reproducible features, although SIFT feature descriptors are typically used to process image pairs with global statistical dependencies of similar intensities. However, these features (e.g., extracted using algorithms such as SIFT or SURF) usually do not match multimodal images with significantly different intensities. To ensure the generality of the approach, features are extracted from edge maps, which are common in retinal images.

The algorithm will consider the pixels in the 3×3 area of the same order of the candidate key point and a total of 26-pixel areas in the upper and lower 2 orders. The point will be considered as a key point if its pixel gray level satisfies the local maximum or minimum. In the SIFT algorithm, there is a value related to the contrast, which we call the SIFT contrast threshold. If the contrast of a key point is less than the threshold we set, the algorithm considers that point to have a lower contrast. If a key point is at the edge of the image or has low contrast, it is eliminated to improve the reliability of the algorithm. The third step is to determine the main direction based on the local structure of each key point. First, the direction of the key point is given a certain value, and then the gradient direction is determined based on the gradient information of the pixels around the point, and then the gradient direction histogram is constructed. The

larger value in the histogram will become the main direction of the key point. The SIFT algorithm centres on the feature point and accumulates the size and direction of the feature point into a histogram and finally obtains a 128-dimensional feature vector, which is used to represent the gradient and grayscale distribution information of the region. The last step constructs a local feature descriptor based on the image gradient in the local neighbourhood of each key point, as shown in Figure 2.

Since SIFT feature descriptors determine the location of key points, the SIFT algorithm determines the feature points in an image based on the grayscale distribution in the image. The extracted feature descriptors contain both geometric and grayscale information [20]. The feature points it extracts are unique and the feature points are robust to image translation, scaling, rotation, radiometric distortion, a large amount of noise, and illumination changes, making it possible to extract feature points for correct matching in a large amount of image data. Therefore, it has wide application value. Here we are only interested in how to obtain the deformation coefficient matrix. To solve for the deformation coefficient matrix, we introduce the energy function, convert it into a negative log-likelihood and minimize it, and finally obtain the variance of the deformation coefficient matrix and the Gaussian mixture model by deriving it. To ensure the spatial structure of the point set during the transformation, we add two geometric structure similarity constraints to this process. We use the spatial transformation function to change the spatial position of the source point set so that it approximates the position of the target point set step by step. There are two quantities involved in the spatial transformation function, one of which is the Gaussian kernel function and the other is the deformation coefficient matrix.

First, an integration operation is performed on the input data to obtain an integral image of the original data. After the integral image is obtained, the scale space of the original data is obtained using the convolution operation, which enables the data to be scale-invariant in the subsequent operations. And all the detected points of interest are based on these scale spaces of different sizes. Secondly, the Hessian matrix determinant is used to detect the speckle. That is, the Hessian matrix operation is performed on the images of each layer in the scale space, and the Hessian matrix can be written as

$$\begin{bmatrix} B - MC^{-1} * M^T & 0 \\ M^T - B & C \end{bmatrix} \cdot \begin{bmatrix} \Delta x^2{}_C \\ \Delta x^2{}_P \end{bmatrix} = \begin{bmatrix} v - M^T C^{-1} \\ w \end{bmatrix}. \quad (1)$$

To find the extreme value of the Hessian matrix, we need to solve G determinant, so the approximate Hessian matrix determinant can be written as

$$G_i\left(\|x - \ell_i\|\right) = \exp\left[\frac{-\|x_i^2 - \ell_i\|^2}{\eta_i^2}\right], \quad i = 1, 2, ..., N. \quad (2)$$

Then, the extreme value suppression operation is performed in a scale-space domain of size $3 \times 3 \times 3$, i.e., the central pixel point is compared with the values of its 26 surrounding nearest neighbours, and the largest or smallest extreme pixel point is selected. Finally, the Taylor formula is
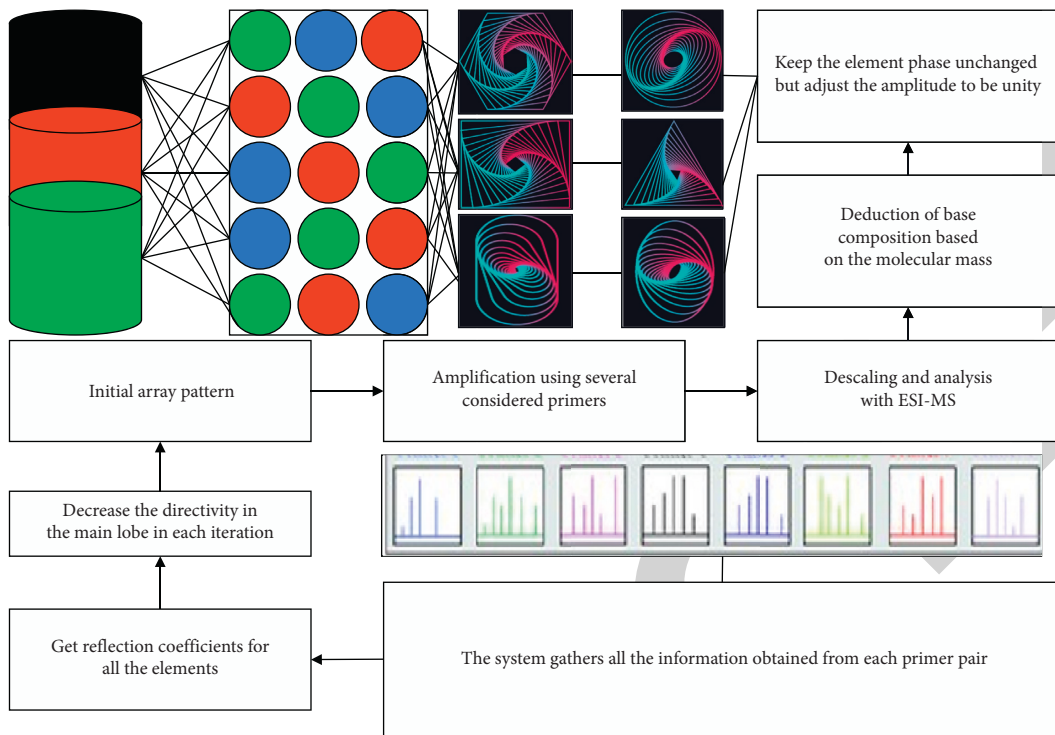
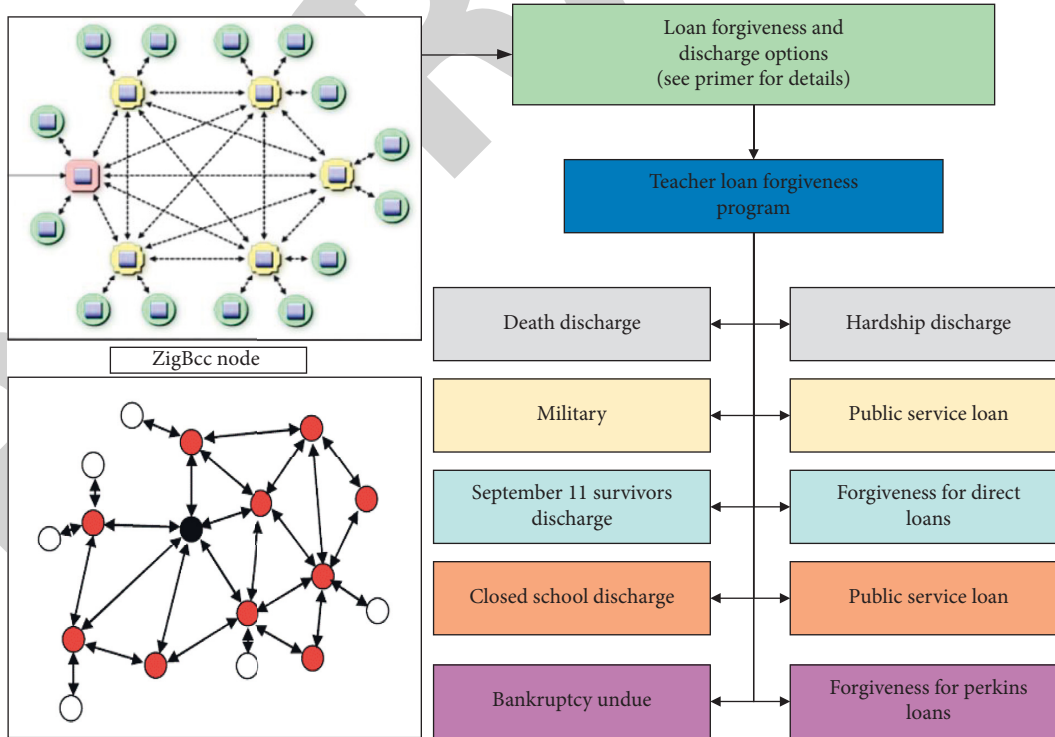Figure 1: Geometric transformation algorithm design.

Figure 2: Schematic diagram of the working principle of local geometric structure constraint.

chosen to fit the surface function, and the point of interest is extracted accurately, and the position (b, w) of the point of interest is obtained with ϕ. At this point, the operation of feature point detection on the input data can be completed.

$$\phi^* = \arg\max\left\{\sup_{x\in\Omega_x}\left|b^2(x) - W^T S(x)\right|\right\},$$

$$\partial_1\|c\|^2 \geq \int_{t_0}^{t_0+T_0}\left|S_1^T(\tau)c\right|^2 d\nu(\tau) \geq \partial_2\|c\|^2, \quad \forall_{t_0} \geq 0,\, c \in R^n.$$

(3)

The correspondence is first estimated by measuring the MLF descriptors between two feature point sets using a Gaussian mixture model (GMM), and then the probability density of the GMM is solved using an approximate solution to the correspondence evaluation problem.

$$_a^G D_t^\nu f(t) = \lim_{h\longrightarrow 0}\frac{1}{\varphi^\nu}\sum_{m=0}^{\left[\frac{t-a}{h}\right]}(-1)^m\frac{\Gamma(\nu+m)}{m!\Gamma(\nu-m+1)}f^\nu(t-mh).$$

(4)

After obtaining the PDF of the GMM induced by MLF, the correspondence is estimated by computing the posterior probabilities of the GMM according to Bayes' rule.

$$-\text{div}\left(\frac{\nabla^a u^2}{|\nabla^a u^2| + p}\right) + \lambda_e\left(u - u^2\right) = 0.$$

(5)

After obtaining the correspondence matrix between the two feature point sets, the spatial transformation of the source feature point set X is updated in this step based on this matrix. Since the source feature point set is constructed as a GMM, the spatial transformation update is done by obtaining the optimal values of the GMM parameters. Therefore, the spatial transformation update of the nonrigid alignment can be viewed as a parameter optimization process, i.e., finding the optimal parameter matrix of the GMM by minimizing the negative log-likelihood function of equation (5), which is shown as follows.

$$M^* = \arg\max\left\{\sup_{x\in\Omega_x}\left|b(x) - W^T S(x)\right|\right\}.$$

(6)

The expectation-maximization (EM) algorithm is used to solve this optimization problem. The EM algorithm consists of two steps, calculating the posterior probability (E step) and maximizing the expectation (M step).

$$\phi \leq \sqrt{qh} = \frac{\sqrt{q}}{2^*}\min_{i\neq j}\left\|\ell_i - \ell_j\right\| \leq 0.$$

(7)

Feature extraction is performed on the preprocessed images. We use the EOH-SIFT feature extraction algorithm to complete the feature extraction process for the preprocessed image to be aligned and the reference image [21]. The left side shows the feature points extracted from the image to be aligned, and the right side shows the feature points extracted from the reference image. The extraction and combination of multiple features can fully describe the features, facilitate the subsequent feature similarity comparison, and improve the robustness and accuracy of feature alignment.

$$Q_N(w) = \frac{1}{2}\sum_{i,j}P_{ij}\left(1 - P_{ij}\right)^2 + \left\|w^T X_b w\right\|_2^2 + X_b w,$$

(8)

$$\frac{\partial L}{\partial\beta_j} = \sum_{i=1}^n\left[y_i - \frac{\exp\left(a + \sum_{j=1}^m x_{ij}^2\beta_j^2\right)}{1 + \exp\left(a + \sum_{j=1}^m x_{ij}^2\beta_j^2\right)}x_{ij}^2\right] = 0, \quad j = 1, 2, \ldots, m.$$

We use a combination of EOH-SIFT features, global geometric structure features, and local geometric features for feature point extraction using the EOH-SIFT algorithm. We use the Euclidean distance for the global geometric features and vector-based feature descriptors for the local geometric features. This is an innovative point of our proposed algorithm. We add the proposed multifeature (MLF) to the Gaussian mixture model, and we consider the set of feature points obtained from the image to be aligned (we call it the source point set) as the set of centres of mass of the mixture model and the set of feature points obtained from the reference image (we call it the target point set) as the data points and find the correspondence between them to simplify the problem of solving the probability density. We mainly use the correspondence matrix to find the correspondence between two-point sets, and the correspondence matrix is obtained by a Gaussian mixture model and Bayesian principle. The particle swarm algorithm simulates the birds in a flock of birds by designing a massless particle. The particles have only two attributes: speed and position. Speed represents the speed of movement, and position represents the direction of movement. Each particle searches for the optimal solution separately in the search space, records it as the current individual extreme value, shares the individual extreme value with other particles in the entire particle swarm, and finds the optimal individual extreme value as the entire particle. All particles in the particle swarm adjust their speed and position according to the current single extreme value found and the current global optimal solution shared by the entire particle swarm.

2.2. Visualization Design of 3D Medical Images of Ocular Blood Vessels. Since fundus photographs acquired by medical devices often contain many images in which blood vessels cannot be identified by the naked eye, these images are wasted in the segmentation network in terms of computing time and are also very likely to affect the accuracy of segmentation, so it is necessary to perform a vessel quality assessment on the images before performing vessel segmentation [22]. The method in this paper uses image processing algorithms to automatically score the clarity of blood vessels in fundus images. Most current studies related to fundus images involve the analysis of fundus vessels, so it is necessary to assess the quality of fundus vessels. Manual assessment of vessel quality is time-consuming and labour-intensive, and individual variability makes it undesirable in practical clinical applications. Automated assessment of vascular quality usually requires the use of large sample sizes of training data. However, no dataset exists for fundus vascular quality assessment, making it difficult to apply supervised learning methods, including deep learning. And traditional image evaluation systems usually evaluated for features such as image noise do not apply to vascular quality. The flow of the evaluation system in this scheme is shown in Figure 3. The evaluation system on the one hand gets rid of the dependence of supervised learning methods on training datasets and on the other hand discards the limitation of traditional image evaluation systems that only evaluate for image noise and other features, effectively solves the problem of automatic assessment of blood vessel quality, and provides a strong basis for fundus image research.

After completing the initial stage, the next stage is the iterative stage. Since there are already some reconstructed 3D points in space, a new view (called view three) is added at this time, and view three and view two are matched due to the ordered image set; those matching points between view three and view two that have completed the reconstruction of 3D points in space can be searched for, and the camera pose of view three can be calculated using the correspondence between these 2D points and their 3D points, and then the pose of view three and view two can be triangulated. The remaining matching points are reconstructed. This process is repeated until all the views are rebuilt. After 6 iterations and 10 iterations, the processed reconstruction result can be obtained [23]. The point cloud results are continuously dense and the model reduction is gradually increasing. After all the views have been calculated, the iteration phase is finished. At this point, the complete spatial point cloud coordinates are obtained, but there are still some errors in them. The reason for this is that in the process of recovering the spatial point coordinates, the solution of the eigenmatrix, camera pose, and triangulation is theoretically inaccurate at the time of calculation. This error will be further accumulated after more images are added in successive iterations, which affects the final reconstruction quality. Therefore, the algorithm needs to process this result to minimize the reprojection error. Since the derivative function matrix of the 3D reprojection problem is sparse, the efficiency of the beam levelling method is ideal here, as shown in Section 2.1. After the error minimization process, the result is the final output.

Preprocessing is the feature extraction and matching work for the input image. The input of this part is the original image, and the feature extraction algorithm based on the scale-invariant feature transform with the improved feature matching process is used. The matching relationship between the feature points of the output image and the adjacent images is obtained. The spatial point reconstruction part is based on the result of feature matching using peripolar geometric constraints to recover the camera pose and then completes the spatial point reconstruction using this camera projection matrix and triangulation. This part is divided into two stages: initial reconstruction and iterative reconstruction. The first input is the feature points of the image and the feature point matching relationship between neighbouring images, and then the random sample consensus (RANSAC) algorithm is used to further filter the matching results and filter out the matching pairs that meet the peripolar geometric constraints and enter the initial reconstruction stage. At this time, the camera projection matrix is calculated by calculating the camera eigenmatrix, and then the initial spatial point reconstruction is completed by this projection matrix and triangulation. Next, we enter the iterative reconstruction phase. At this time, the reconstructed spatial 3D points are combined with 2D feature points to recover the poses of the newly added view cameras, and the remaining matching points in the new view are reconstructed using the camera pose information. This process is iterated until all the views have been calculated. The coordinates of all calculated 3D point clouds and the recovered camera projection matrix are output, as shown in Figure 4.

Finally, this reconstruction result is reprocessed and the final output is obtained by minimizing the reprojection error using beam levelling. The input of this part is the reconstructed 3D point cloud coordinates and the camera projection matrix [24]. The reconstructed 3D points are projected to the image plane using the projection matrix, and the resulting image plane coordinates will be in error with the left side of the initial plane. The point cloud coordinates and the camera projection matrix are jointly adjusted by the beam levelling method to minimize this error, and the point cloud coordinates are then more accurate. The result of this process is output. The body plotting algorithm is to process each voxel in the 3D data field and map the data of the 3D data field to the 2D data plane according to the characteristics of the optical model. The core idea of volume mapping is that each voxel in the 3D data field has reflection, projection, and refraction of light, so the light from the light source may be absorbed or reflected or projected through the voxel, making each voxel have a different light intensity and colour properties, synthesizing all the voxel data and finally synthesizing the data model. The model drawn by the body drawing algorithm can not only reveal the surface information of the object but also highlight the internal structure of the object. Body drawing algorithms include a ray projection algorithm, a sputtering method, shear deformation, snowball throwing method, etc., among which the most widely used is the ray projection algorithm. The basic principle of light projection algorithm is as follows: set each
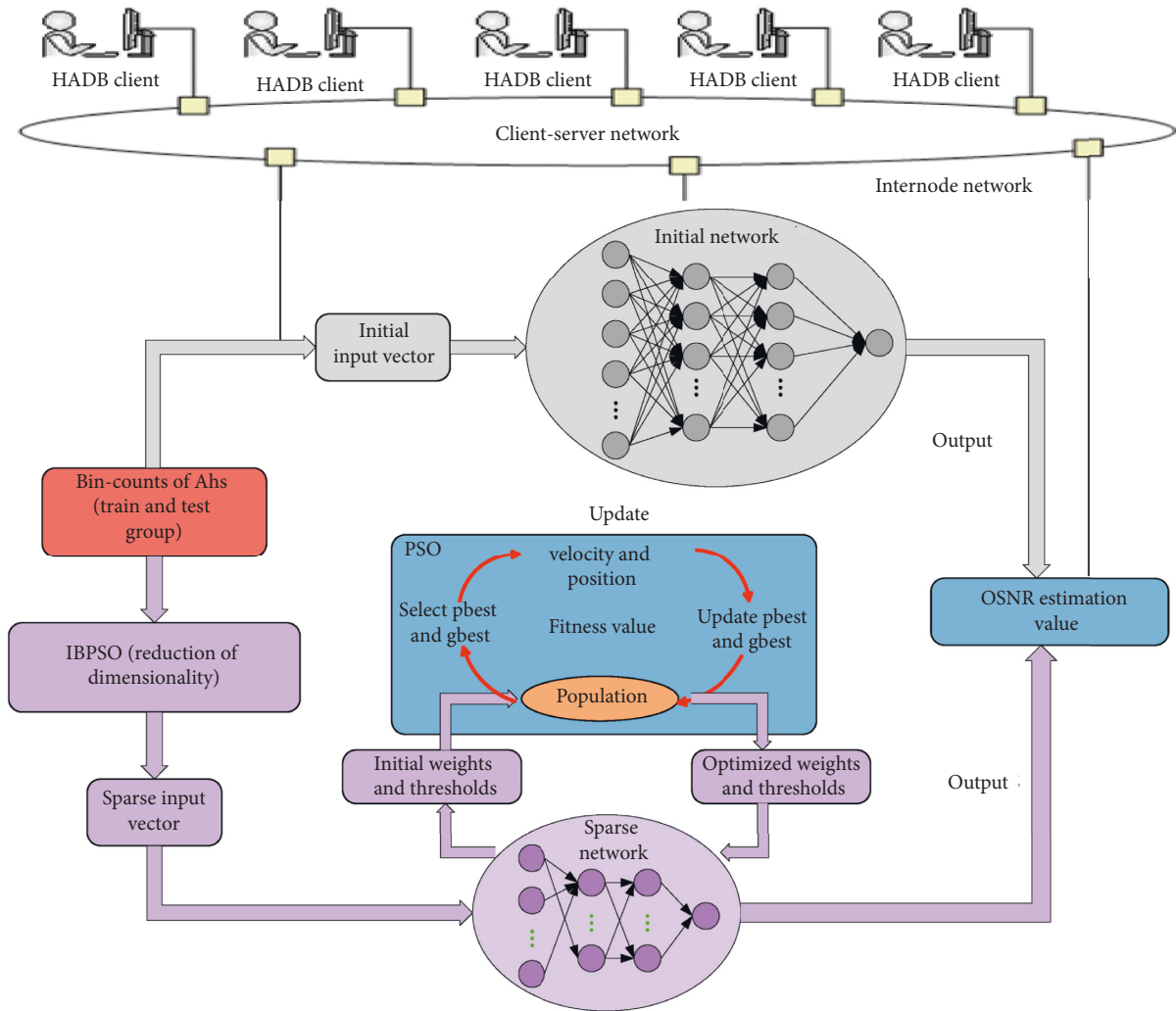
FIGURE 3: Visualization design framework for medical images.

voxel to start with an initial colour value, from the light source, emit a parallel light to each voxel in the 3D data field, the light passes through the 3D data field, then do equal distance sampling for each light passing through the 3D data field, then do three linear interpolations for the 8-pixel points in the spatial neighbourhood of each sampled point, and recalculate the value of each sampled point. Finally, the colour values and opacity of the recomputed sampling points on each ray are summed and synthesized to obtain the final image, as shown in Table 1.

In medicine, the body drawing algorithm, by accumulating the colour and opacity of each voxel, forms a 3D model that can well represent the internal tissues and organs of the human body, but the drawing process takes a lot of time and memory to calculate each voxel, which makes the 3D reconstruction as well as the model rendering slow [25]. Wavelet decomposition is often used in the image processing part of computer graphics, and now it also used in the field of mesh simplification. The basic idea of this algorithm is as follows: the original model is decomposed into two parts—the low-frequency signal and the high-frequency

signal by using wavelet decomposition, the low-frequency signal is a reduced model of the original model, and this part of the signal is obtained by the weighted average of the neighbourhood of the vertices of the original model, and the simplified model consists of a combination of the low-frequency signal and the filtered high-frequency signal. This method is efficient and easy to implement but has a small range of use and high requirements for the model.

3. Analysis of Results

3.1. Analysis of Algorithm Results. The experimental data are obtained from the vascular model by the MC improvement algorithm, which is simplified by the original QEM algorithm and the improved QEM algorithm, and the time consumed by the two algorithms in achieving different simplification effects is recorded in Figure 5.

From Figure 5, we can see the time consumed by different grid models with the simplification rate divided into 20% and 40%, and the comparison shows that the improved algorithm can improve the efficiency of model simplification very well. In
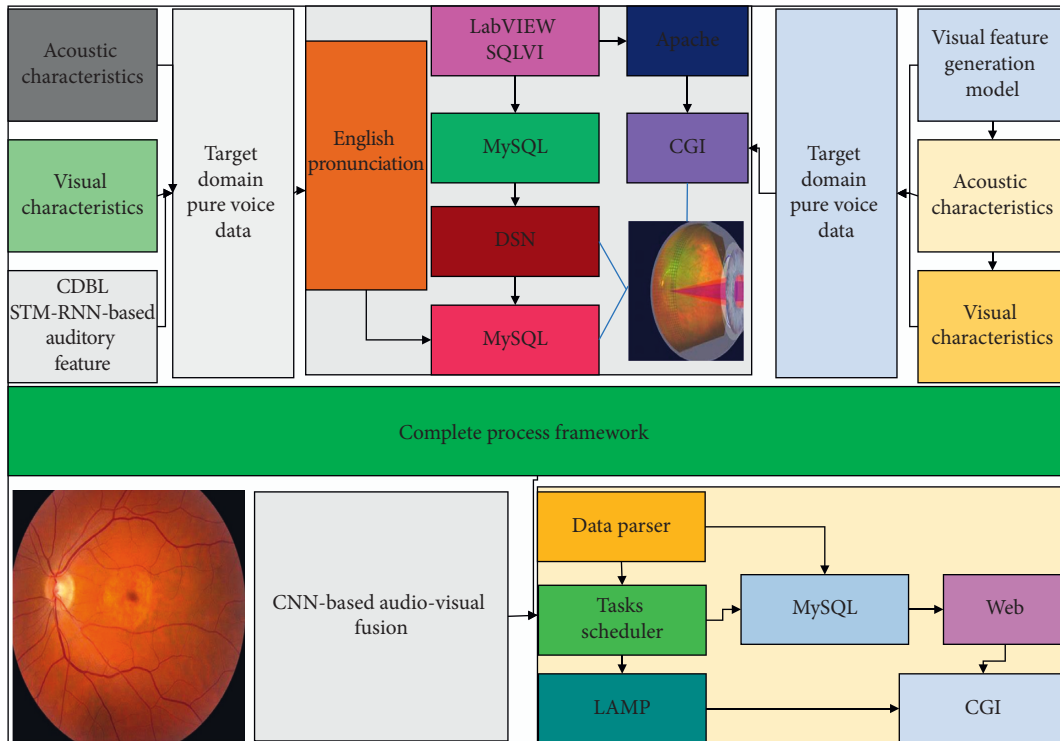
Figure 4: Complete process framework.

Table 1: Algorithm experimental data parameters.

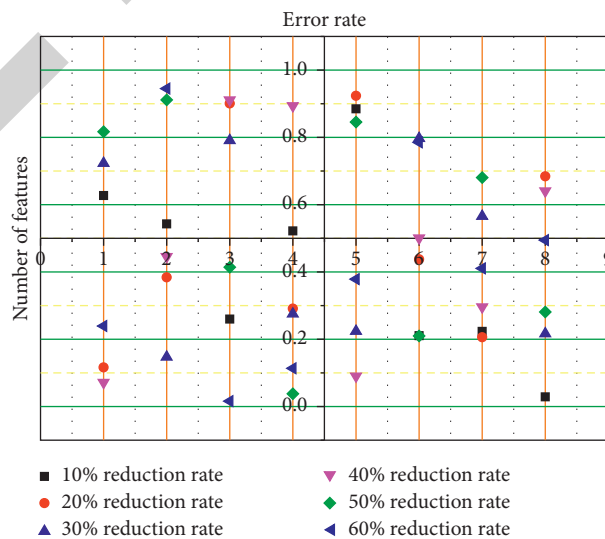| Name	Dinosaur	Corridor	Merton College III	Vercingetorix	Alcatraz
View resolution	75	45	38	47	58
Number of views	4	5	6	7	8
Average value	12.5	9.4	9.9	8.6	1.5
Sum value	50	47	59	60	12

Figure 5: Comparison of the effect of the original and optimized algorithms.

feature-based image alignment, due to the complexity of retinal images (e.g., unavoidable noise, repetitive structures, occlusions, and multimodal data), the alignment process often results in a high percentage of incorrect feature matches. Accurate point matching is a crucial and challenging process. The goal is to establish a reliable correspondence and find the underlying spatial transformation between two sets of feature points (also called key points). For feature-based alignment algorithms, the alignment process involves the feature matching process of points, and good feature matching can lead to better experimental results for subsequent feature point-based image alignment algorithms. Meanwhile, we can use feature matching as a by-product obtained from image alignment. In this way, we can use the number of correct matches and the match rate available for indirect characterization of performance, where the match rate is defined as the ratio of the number of correct matches retained to the total number of matches retained. In our evaluation, the basic facts of match correctness are determined by manual inspection. Although the judgment of correct or incorrect matches seems to be arbitrary, we set benchmarks to ensure objectivity.

We perform experiments using four different retinal image pairs to test the ability of the method in terms of feature matching. The evaluation criterion we use is the match rate, comparing our method with GLMD, VFC, SIFT, CPD, and RSOC. The match rate is defined as the ratio of the number of correct matches retained to the total number of matches retained. The results of the quantitative comparison are shown in Figure 6. The results show that our method provides the best performance in each group of experiments and has the highest average feature matching rate. This facilitates the accurate estimation of the transformations.

Experiments were performed using 100 pairs of retinal images. These images with different imaging modalities have large intensity variations. First, the intuitive results of the method are given by the three typical retinal image pairs in Figure 6. For each pair of experiments, the first row is the original retinal image pair, and the corresponding edge maps are placed on the next row. As can be seen from the figure, some tissues in the retinal image pairs, especially the blood vessels and optic nerve discs, have very different intensity structures. However, their corresponding edge maps are very similar. Therefore, the algorithm can align multimodal retinal images by matching their edge maps with EOH-SIFT features. The third row shows the results of EOH-SIFT feature matching. The left and right sides of the last row present the transformed image and the tessellation of the target image, respectively.

The mean and standard deviation of RMSE, SD and MAE of the entire data set are shown in Figure 7. The methods have the best performance in all cases compared to SIFT, CPD, GLMDTPS, VFC, and RSOC. The average running time of the five methods after excluding the cost of EOH-SIFT feature extraction on the test data is shown in Figure 7. In the absence of the cost of EOH-SIFT feature extraction, VFC is the most efficient algorithm in terms of average running time compared to the other five methods, but there is no doubt that the performance of the methods is still competent for the experiments.

The evaluation was performed using 100 retinal image pairs from multiple views, where 30 retinal image pairs with less than 50% overlap were selected from the entire dataset to make the test data more challenging. Similarly, the intuitive results of the method are given by the three typical retinal image pairs in Figure 7. Clearly, the effect of the continuous vessels in the checkerboard and the alignment overlap in the mosaic shows that the method of this paper can produce so many correct feature matches that the retinal image pairs can be accurately aligned. Since the same modal capture is used, it is known that edge map extraction may not be necessary for multiview retinal image alignment. Nevertheless, this paper still uses the edge map for experimental consistency.

3.2. Analysis of Visualization Results. It is easy to find that the blood vessels in the fundus image are concentrated near the optic disc, and the blood vessels far away from the optic disc are usually very small, while the blood vessels inside the optic disc are disjointed, both of which are difficult to identify. Therefore, we consider a circular region with the centre of the optic disc as the region of interest (ROI), as shown in Figure 8. It is now necessary to determine how much the inner and outer diameters of the circle are more meaningful for medical diagnosis.

Regarding the selection of the inner and outer diameters of the ROI, we considered the region of interest for morphological analysis by adjusting the morphological analysis of the fundus images of the patient population and the healthy population to identify the region in which the analysis results of the patient population showed the most significant difference from the analysis results of the healthy population. To provide effective data support for the subsequent medical diagnosis, we finally selected the annular region of interest from 4-fold optic disc radius to 10-fold optic disc radius or 12-fold optic disc radius as the region of interest for morphological analysis. Among them, we finally selected the annulus with a 4× to 10× optic disc radius as the region of interest.

The optic nerve head (ONH) transmits visual information from the retina to the brain. It acts as the central retinal artery and central retinal vein into the entrance and exit areas of the eye, providing nourishment to the retina. The ONH has a central part called the optic cup, which is responsible for diagnosing glaucoma. Glaucoma is the second leading cause of vision loss in the world. Glaucoma changes the shape of the cup region. Therefore, the cup-to-disc ratio (CDR) is a parameter that can be used as an early indicator of glaucomatous abnormalities. The progressive intensity changes between the optic cup and the neuroretina rim (periocular region) ends at the disc border, which can lead to other complications of using image processing methods for cup segmentation.

To verify its advantages, a quantitative comparison in terms of sensitivity (Sn) was performed with the random resonance results in the global sense. When the first expert's manual segmentation results were used as the standard, the average value of random resonance results in the global sense was Sn = 0.5005, while the average value of results
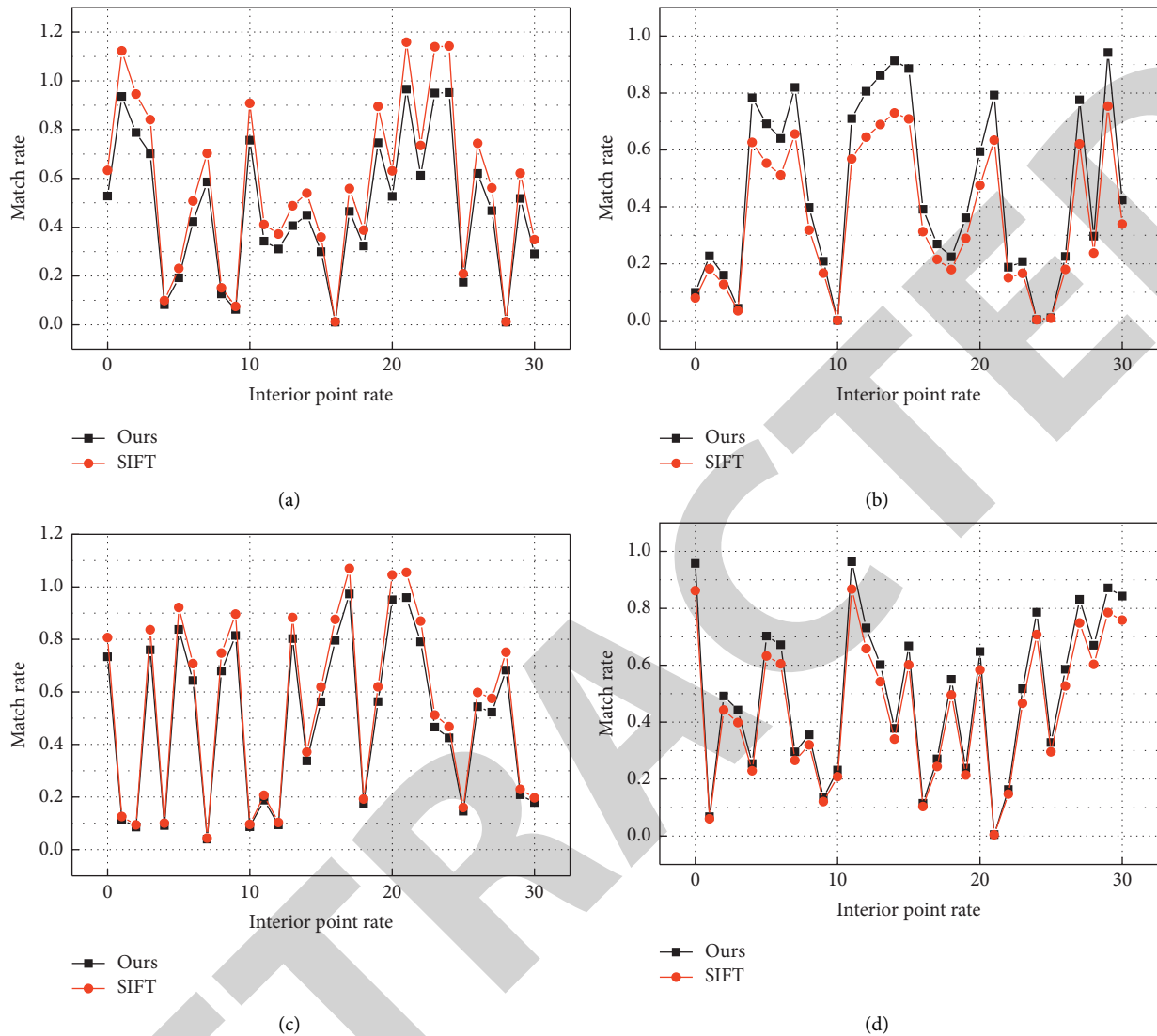
(a)

(b)

(c)

(d)

Figure 6: Feature matching results of different algorithms on different types of retinal images.

obtained by the multilevel segmentation method was Sn = 0.7012, and the difference between the two was 0.2007. When the second expert's manual segmentation results were used as the standard, the average value of random resonance results in the global sense was Sn = 0.5210, and the average value of results obtained by the multilevel segmentation method was Sn = 0.7027, and the difference between the two was 0.1817. From the data displayed in Figure 9 and the difference in the mean values, it can be seen that the sensitivity of the multilevel segmentation method in proposed in this paper is significantly improved compared with the global random resonance results, indicating that the method proposed in this paper has obvious advantages in the segmentation of vessels with low-intensity levels.

The vessel diameter measurements were performed on KPIs and VDIS in the REVIEW database. The proposed method has the smallest mean diameter difference and the smallest standard deviation from the results of the vessels of the gold standard compared to the prior art, demonstrating the high practical value and accuracy and high stability of the proposed method. Many systemic diseases can cause changes in retinal vessel diameter, and the small artery-to-vein diameter ratio (AVR) is an important quantitative biomarker for the diagnosis of these diseases. We propose and validate a novel automated retinal vessel diameter measurement method. Considering the binary segmentation of the fundus, a morphological approach is first used to extract the centreline of the retinal vessels, which is then used to determine the location of points in the vessels. Then, the Hessian matrix was used to determine the initial orientation of the vascular skeleton points. Finally, the vessel diameter is measured based on the determined vessel centreline and orientation information. The method performs better compared to several existing techniques.
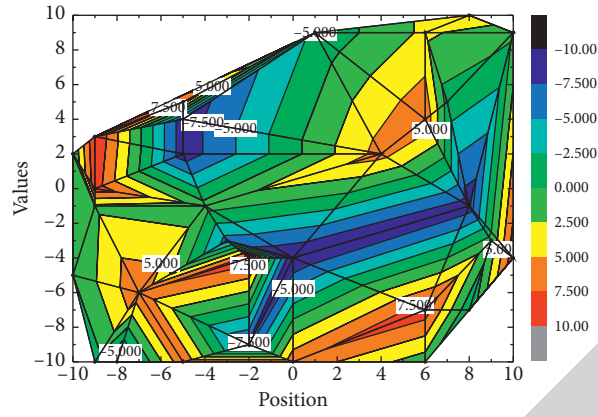
Figure 7: Comparison of the average running time of different algorithms in aligning multimodal retinal images.
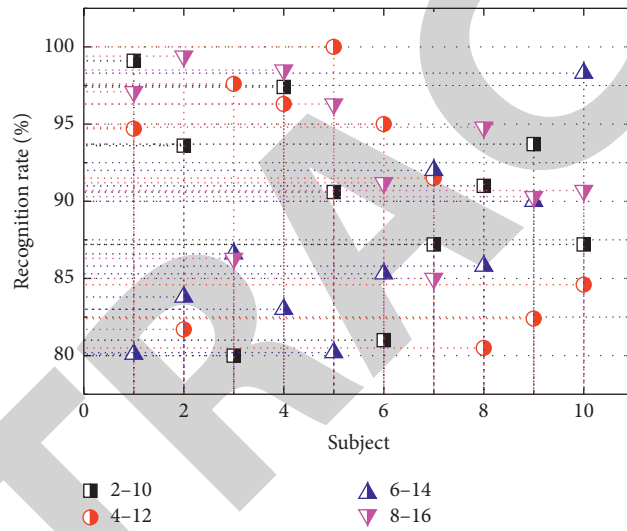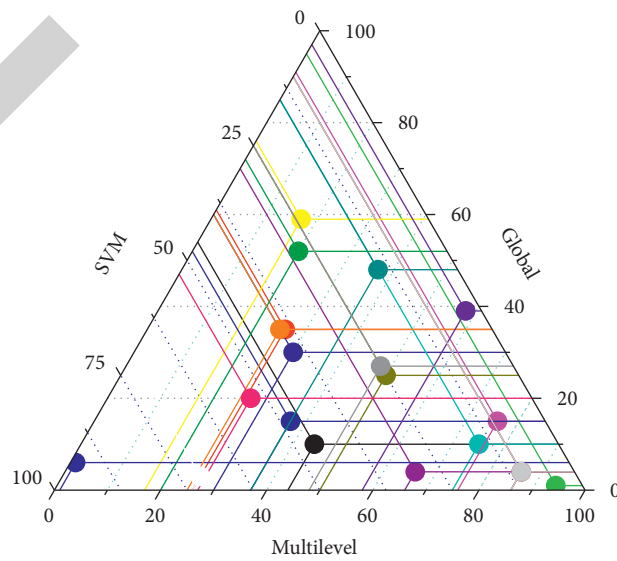

Figure 8: Results of t-test.

Figure 9: Comparison of the sensitivity of the results.

4. Conclusion

The geometric transformation algorithm approach uses separable spatial and channel flow and dense adjacent vessel prediction to capture the maximum spatial correlation between vessels. Image preprocessing is performed to enhance retinal vessel contrast. Geometric transformations and overlapping patches are used in both the training and prediction phases to efficiently utilize the information learned in the training phase and to refine the segmentation. The uncertainty of each pixel in the training phase is estimated approximately, and then a smaller uncertainty is used to guide the subsequent segmentation network. We formulate a modified cross-entropy loss function. The Γ-convergence of such new models is explored, and the 2D and 3D numerical results show that the models have better segmentation results. Then, the segmentation model based on the coupled model of the phase-field model and deep learning model is a research direction worth exploring. Because the phase-field model does not require too much convolution operation when segmenting 3D brain images, thus saving some segmentation time, it is a valuable research problem if the deep learning model is used as a preprocessing step that may enhance the features of its segmented images, which can save segmentation time on the one hand and improve the segmentation accuracy on the other hand. Also, we design a building block called an inflated starting block (DIB) to better generalize the model of interest and extract multiscale features more efficiently. The various segmentation algorithms proposed in this paper have good segmentation performance, and the various morphological analysis methods proposed have more practical application potential. It plays a role in promoting the application of fundus image analysis in computer-aided disease diagnosis systems. In the future, we will conduct more in-depth research and discussion.

Data Availability

The data used to support the findings of this study are available from the corresponding author upon request.

Conflicts of Interest

The authors declare that they have no conflicts of interest.

References

[1] M. Arif and G. Wang, "Fast curvelet transform through genetic algorithm for multimodal medical image fusion," *Soft Computing*, vol. 24, no. 3, pp. 1815–1836, 2020.

[2] Y. Huang, G. Hu, C. Ji, and H. Xiong, "Glass-cutting medical images via a mechanical image segmentation method based on crack propagation," *Nature Communications*, vol. 11, no. 1, pp. 1–15, 2020.

[3] D. Maji and A. A. Sekh, "Automatic grading of retinal blood vessel in deep retinal image diagnosis," *Journal of Medical Systems*, vol. 44, no. 10, pp. 1–14, 2020.

[4] W. G. O'Dell, A. K. Gormaley, and D. A. Prida, "Validation of the gatortail method for accurate sizing of pulmonary vessels from 3D medical images," *Medical Physics*, vol. 44, no. 12, pp. 6314–6328, 2017.

[5] G. Du, X. Cao, J. Liang, X. Chen, and Y. Zhan, "Medical image segmentation based on U-net: a review," *Journal of Imaging Science and Technology*, vol. 64, no. 2, pp. 20508–20512, 2020.

[6] S. Jeon, H. B. Song, J. Kim et al., "In Vivo photoacoustic imaging of anterior ocular vasculature: a random sample consensus approach," *Scientific Reports*, vol. 7, no. 1, pp. 1–9, 2017.

[7] P. Afshar, A. Mohammadi, K. N. Plataniotis, A. Oikonomou, and H. Benali, "From handcrafted to deep-learning-based cancer radiomics: challenges and opportunities," *IEEE Signal Processing Magazine*, vol. 36, no. 4, pp. 132–160, 2019.

[8] V. Muneeswaran and M. P. Rajasekaran, "Automatic segmentation of gallbladder using bio-inspired algorithm based on a spider web construction model," *The Journal of Supercomputing*, vol. 75, no. 6, pp. 3158–3183, 2019.

[9] X. Zhang, W. Chen, G. Li, and W. Li, "The use of texture features to extract and analyze useful information from retinal images," *Combinatorial Chemistry & High Throughput Screening*, vol. 23, no. 4, pp. 313–318, 2020.

[10] F. Alam, S. U. Rahman, S. Ullah, and K. Gulati, "Medical image registration in image guided surgery: issues, challenges and research opportunities," *Biocybernetics and Biomedical Engineering*, vol. 38, no. 1, pp. 71–89, 2018.

[11] D. Motta, W. Casaca, and A. Paiva, "Vessel optimal transport for automated alignment of retinal fundus images," *IEEE Transactions on Image Processing*, vol. 28, no. 12, pp. 6154–6168, 2019.

[12] P.-H. Lee, C.-C. Chan, S.-L. Huang, A. Chen, and H. H. Chen, "Extracting blood vessels from full-field OCT data of human skin by short-time RPCA," *IEEE Transactions on Medical Imaging*, vol. 37, no. 8, pp. 1899–1909, 2018.

[13] V. Satyananda, K. V. Narayanaswamy, and K. Karibasappa, "Hard exudate extraction from fundus images using watershed transform," *Indonesian Journal of Electrical Engineering and Informatics (IJEEI)*, vol. 7, no. 3, pp. 449–462, 2019.

[14] J. Zhang, Y. Qiao, M. S. Sarabi et al., "3D shape modeling and analysis of retinal microvasculature in OCT-angiography images," *IEEE Transactions on Medical Imaging*, vol. 39, no. 5, pp. 1335–1346, 2019.

[15] D. A. Da Rocha, A. B. L. Barbosa, D. S. Guimarães et al., "An unsupervised approach to improve contrast and segmentation of blood vessels in retinal images using CLAHE, 2D Gabor wavelet, and morphological operations," *Research on Biomedical Engineering*, vol. 36, no. 1, pp. 67–75, 2020.

[16] S. S. Joseph and A. Dennisan, "Three dimensional reconstruction models for medical modalities: a comprehensive investigation and analysis," *Current Medical Imaging Formerly Current Medical Imaging Reviews*, vol. 16, no. 6, pp. 653–668, 2020.

[17] L. E. Carvalho, A. C. Sobieranski, and A. Von Wangenheim, "3D segmentation algorithms for computerized tomographic imaging: a systematic literature review," *Journal of Digital Imaging*, vol. 31, no. 6, pp. 799–850, 2018.

[18] A. Taruttis, A. C. Timmermans, P. C. Wouters, M. Kacprowicz, G. M. Van Dam, and V. Ntziachristos, "Optoacoustic imaging of human vasculature: feasibility by using a handheld probe," *Radiology*, vol. 281, no. 1, pp. 256–263, 2016.

[19] H. Zhao, N. Chen, T. Li et al., "Motion correction in optical resolution photoacoustic microscopy," *IEEE Transactions on Medical Imaging*, vol. 38, no. 9, pp. 2139–2150, 2019.

[20] M. Paknezhad, S. Y. M. Loh, Y. Choudhury et al., "Regional registration of whole slide image stacks containing major histological artifacts," *BMC Bioinformatics*, vol. 21, no. 1, pp. 1–20, 2020.

[21] B. Liu, C. Zhu, X. Qu et al., "A cerebrovascular image segmentation method based on geometrical feature point clustering and local threshold," *Current Medical Imaging Reviews*, vol. 14, no. 5, pp. 748–770, 2018.

[22] L. Ji, X. Jiang, Y. Gao, Z. Fang, Q. Cai, and Z. Wei, "ADR-Net: context extraction network based on M-Net for medical image segmentation," *Medical Physics*, vol. 47, no. 9, pp. 4254–4264, 2020.

[23] F. K. S. Chan, X. Li, and A. W.-K. Kong, "A study of distinctiveness of skin texture for forensic applications through comparison with blood vessels," *IEEE Transactions on Information Forensics and Security*, vol. 12, no. 8, pp. 1900–1915, 2017.

[24] V. Deepa, C. Sathish Kumar, and S. Susan Andrews, "Automated detection of microaneurysms using Stockwell transform and statistical features," *IET Image Processing*, vol. 13, no. 8, pp. 1341–1348, 2019.

[25] J. De Moura, J. Novo, P. Charlón, N. Barreira, and M. Ortega, "Enhanced visualization of the retinal vasculature using depth information in OCT," *Medical & Biological Engineering & Computing*, vol. 55, no. 12, pp. 2209–2225, 2017.